J. Fluid Mech. (1998), *vol.* 372, *pp.* 189–212. Printed in the United Kingdom

The role of surface disturbances in the entrainment of bubbles by a liquid jet

By HASAN N. OĞUZ

Department of Mechanical Engineering, The Johns Hopkins University, Baltimore MD 21218, USA

(Received 30 August 1997 and in revised form 10 May 1998)

In this paper, air entrainment by a liquid jet is studied. The size of bubbles entrained by jets plunging into a liquid can be consistently decreased to the 50–100 μm range, and their number increased in a highly controllable fashion, by surrounding a mm-size jet by a hollow cap with a slightly larger inner diameter. When the right amount of air is supplied to the cap, small air bubbles detach from a steady annular cavity that forms around the jet and are entrained into the liquid. The fluid mechanical principles underlying this interesting and useful effect are investigated experimentally and theoretically in this paper. It is shown that a key aspect of the process is the jet surface roughness, which is studied quantitatively and explained in terms of the boundary layer instability inside the nozzle. The maximum bubble size is found to be nearly equal to one quarter of the wavelength of the jet surface disturbances, consistent with a breakup process of relatively large air pockets around the jet, as suggested by close-up pictures. The average bubble size downstream of the cap increases proportionally to the air to water flow ratio. Boundary integral simulations of the air pocket formation are carried out. The results are found to be useful in explaining important characteristics of the experiment such as the threshold for entrainment and cavity size.

1. Introduction

The production of gas bubbles constitutes an important as well as a costly component in a wide variety of industrial applications such as gas–liquid reactors (Burgess, Molloy & McCarthy 1972) biological reactors (Boulton-Stone & Blake 1993), purification of liquids (Dixon *et al.* 1991), waste water treatment (Tchobanoglous & Burton 1991), and fish pond aeration (Tucker & Robinson 1990). In other cases of practical importance, such as flotation columns, it is the buoyancy of the gas bubbles that produces the desired effect. Bubbles are also known to be excellent underwater acoustic shock absorbers that can be used as a protection from a nearby explosion. The common point of the aforementioned applications is that they all require small bubbles to be generated in large quantities. The classical way of accomplishing this task is to force gas through a submerged orifice and has been extensively studied in the literature. Excellent reviews have been given by Ramakrishnan, Kumar & Kuloor (1969) and Satyanarayan, Kumar & Kuloor (1969). The interest in the subject has been high over the years (e.g. Marmur & Rubin 1976; Blanchard & Syzdek 1977; Tsuge, Hibino & Nojima 1981; Baker & de Nevers 1984; Pamperin & Rath 1995). Gas bubbles in liquids can also be efficiently produced by directing a liquid jet at a liquid surface. Although the process of air entrainment by a liquid jet has been

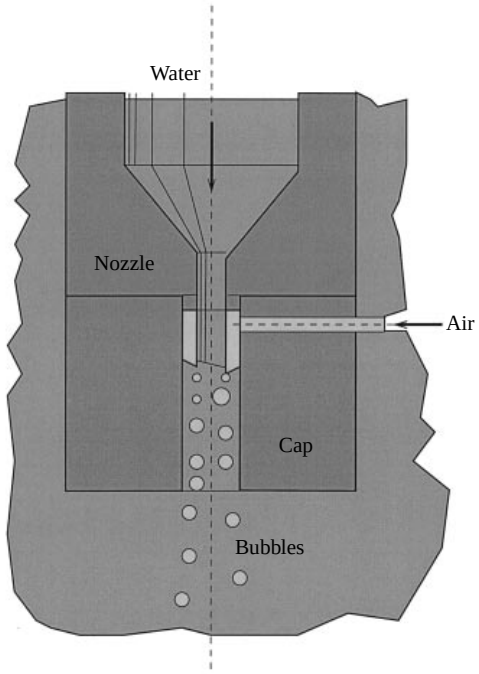

FIGURE 1. Schematic description of the small bubble generation technique by a nozzle fitted with a hollow cap.

investigated for a long time, its industrial use has been limited probably due to the incomplete understanding that has been achieved.

The earliest study of air entrainment by a liquid jet is by Lin & Donnelly (1966). They observed that disturbances on the jet surface are primarily responsible for the air entrainment process in the case of turbulent jets. This is in contrast to very viscous jets where the breakup of a thin film between the jet and the receiving liquid is the dominant mechanism. Subsequent publications confirmed this hypothesis and several empirical relations describing the entrainment rate have been proposed. McCarthy, Henderson & Molloy (1970) related the jet surface roughness to the air entrainment rate. Motivated by this finding, Burgess, Molloy & McCarthy (1972) examined the effect of the nozzle geometry. Van de Sande & Smith (1973) considered the limit of high speed jets and found a new regime of continuous entrainment where the gas boundary layer around the jet cannot be ignored. In a subsequent publication they studied lower velocity jets and established two regimes based on the breakup length of the jet (Van De Sande & Smith 1976). Lara (1979) studied the onset of entrainment for jets near the point where they disintegrate into droplets by capillary breakup. Detsch & Sharma (1990) determined the critical angle of entrainment for jets of various air–liquid combinations. Further empirical relations on the entrainment rate have been given by McKeogh & Ervine (1981), Sene (1988), and others. Recently, Bin (1993) gave an exhaustive survey of experimental and theoretical results on gas entrainment by plunging jets.

In this paper we study the fluid dynamical mechanisms underlying a new method by which very small bubbles can be produced in liquids. The principle is similar to plunging jet entrainment except for the fact that the nozzle from which the jet issues is fitted with a cylindrical cap (figure 1). The cap is hollow with an inner diameter

slightly larger than the nozzle diameter and is flooded with the liquid surrounding the assembly. Air is fed into the cap at the jet exit so that a gaseous annulus is formed around the jet. Along the intersection line between the jet and the liquid in the annulus myriads of bubbles are seen to be entrained into the liquid. Our study shows that this effect is critically dependent on the presence of suitable surface disturbances on the surface of the jet. With this system it is also possible to study in detail this effect that previously has only been considered in a qualitative sense.

The idea of enclosing the jet with a tube is not new and has been proposed to pump gas into a liquid (Cunningham 1974). The maximum depth to which bubbles can travel is limited because the jet slows down considerably due to spreading and turbulent dissipation in the liquid. Ohkawa *et al.* (1986) have shown that it is possible to increase this depth by means of downcomers in air–water systems. Here, the purpose of enclosing the jet is to achieve a better control of the input energy in producing very small bubbles. The nozzle diameter is of the order of a millimetre as opposed to a few millimetres reported by Ohkawa *et al.* (1986). Moreover, the gap between the jet and the enclosing downcomer is in the few millimetres range in their setup, whereas we only have a 400 μm tolerance which enables us to ignore gravitational effects. In our nozzles, the surface tension force alone is enough to keep the air annulus steady in any orientation. Therefore, the nozzle need not be close to vertical or close to the surface. All experiments reported in this paper were performed 5 to 10 cm below the free surface and the orientation did not have any effect on the operation of the nozzle.

There are several subtle points underlying the design of the system described above. The nozzle size is kept small to achieve higher efficiency by inputing the energy to the flow at the right scales. This results in superior performance when compared to traditional techniques of small bubble production. Normally, mechanical agitators are employed to reduce the size of the entrained bubbles (Shah 1992). In order to reduce bubble size the input forcing must have a very short spatial scale. When mechanical agitators are used, the bulk of energy ends up in the long scales. Because of the sharp spectral decay of the energy, the efficiency suffers greatly even though the total energy needed is in fact small. At the other limit, very small nozzles are impractical since they lead to high dissipation losses and are prone to clogging problems. Also, higher speeds are needed in smaller nozzles to produce the same effect since turbulence in the jet is the main driving force.

2. Experimental setup

Experiments were performed in a $75\times45\times30$ cm transparent glass tank filled with tap water (figure 2). Water is circulated with a pump and the flow rate is monitored with a flowmeter (Omega FL 3840) that can measure rates up to 30 ml s^{-1} with an accuracy of $\pm$ 0.3 ml s^{-1}. A laboratory air supply line equipped with a pressure regulator set at 20 p.s.i. is used as the source of gas to ensure a steady flow rate. The flow meter (Omega FL 3445) attached to this line has a range of 0–1.3 ml s^{-1} with an accuracy of $\pm$ 0.03 ml s^{-1}. Tygon tubing is used for water as well as air delivery to the nozzle. The inner diameters are 0.8 and 9.5 mm for air and water respectively. Nozzles of various types are fabricated from aluminium. All caps are machined from acrylic cylindrical blocks and polished for a better view of the interior. The cap's inner wall is coated with a thin layer of wax to create a hydrophobic surface. The air cavity has been observed to be unsteady without this treatment.

Still images of the nozzle and the bubbles were captured with a digital CCD camera

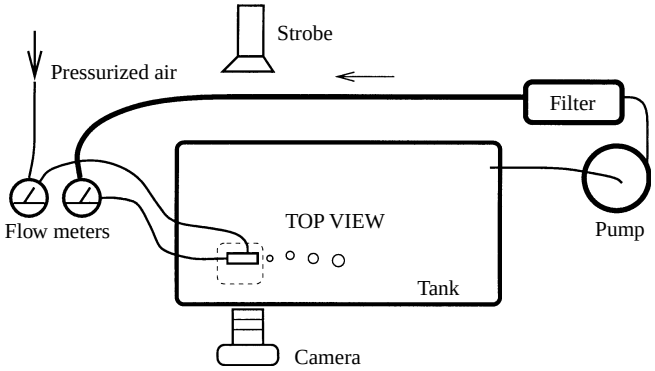

FIGURE 2. Experimental setup.

(Pulnix 9700) that has a resolution of 780×480 pixels. We have used a 55 mm Micro Nikon lens in conjunction with an extension ring (Nikon PK13). For the purpose of measuring bubble size distribution we have set the camera to its highest magnification achieving a resolution of 7.3 μm per pixel horizontally and 8.4 μm per pixel vertically. These numbers are obtained by taking the picture of a ruler and counting pixels over a length of 5 mm. A 35 mm Nikon F3 camera has also been employed in the earlier phase of this work. Pictures were taken with the high speed Kodak film T1000 and the negatives were digitized with Nikon Coolscan digitizer (max 2700 d.p.i.). Even though higher resolution can be obtained in this way, the turn-around time associated with film processing and digitization makes the acquisition of a large number of pictures impractical.

Illumination is provided by a 6 μs strobe (EGG MV1000) which is placed directly behind the tank. A 4 mm white plastic screen used as a diffuser between the strobe and the camera provided adequate lighting for backlit pictures.

3. Basic description of the process

There are two parameters of importance for a given nozzle geometry: the air and water flow rates. One can identify several regimes of operation for the nozzle by varying these parameters. We first conduct a dimensional analysis and consider the relevant forces acting on the fluid to have a basic understanding of these regimes.

In view of the thinness of the jets (0.8–1.2 mm) and relatively high velocities (6–8 m s^{-1}) gravity is not expected to play a significant role. In fact, the smallest Froude number, $Fr = U_{jet}^2/gR_{jet}$ is around 300, where U_{jet} and R_{jet} are the average velocity and radius of the jet, and g is the gravitational acceleration. Therefore, gravitational effects can safely be ignored.

The role of viscous forces is less clear. Let us consider the case of a steady smooth jet as a base state. This situation arises when the flow is laminar. We ignore all viscous effects in the gas and concentrate on the flow field generated by the jet in the cap. Under the typical flow conditions of this regime the Reynolds number is relatively high (but not so high as to make the jet turbulent) and the jet enters the slug of water in the cap maintaining its integrity for many jet diameters. The jet streamlines separate from the free surface along the intersection of the jet with it and a recirculatory flow develops in the thin liquid-filled gap between the penetrating jet and the cap. If we assume that viscous stresses are of the order of $\mu_{water} U_{jet}/\delta$

where $\delta = R_{cap} - R_{jet}$ is the gap thickness, we can calculate the corresponding surface deformation by forming a balance with surface tension. In this way the radius of curvature R_{curv} of the free surface is found to be

$$\frac{R_{curv}}{\delta} = \frac{\sigma}{\mu U_{jet}}. \tag{1}$$

For the largest velocity, $U = 8.3$ m s^{-1}, this ratio is about 8.4 indicating that the free surface surrounding the jet in the cap is nearly flat. The viscous contribution to surface deformation is therefore negligibly small.

A more detailed analysis to confirm this conclusion can be conducted as follows. The flow field around the jet in the cap is similar to that in a boundary layer with a boundary layer thickness of the order δ. The analogy is based on the fact that the length scale in the direction of the flow, X, is much larger than the length scale normal to the flow, δ. By using well known arguments from boundary layer theory, we deduce that the pressure gradient normal to the boundary layer is small and of the order of $\delta\rho U_{jet}^2/X^2$ where ρ is the density. Here we are interested in the pressure gradient rather than the pressure itself because the gradient is the relevant quantity for surface deformation. The integral of this pressure gradient over the boundary layer thickness is $\mu U_{jet}/X$ assuming that $(\delta/X)^2 = O(1/Re)$ as in boundary layer theory. If a ratio between the pressure difference, $\mu U_{jet}/X$, and the surface tension stress σ/δ is formed, we find a scaled capillary number

$$Ca = \frac{\mu U_{jet}}{\sigma}\frac{\delta}{X}. \tag{2}$$

For the largest velocity, $U = 8.3$ m s^{-1}, this number is found to be $0.12\delta/X$ which is always much smaller than one, indicating the dominance of surface tension force over viscous stresses.

As for the inertial forces, they do not participate significantly in the deformation of the free surface in this ideal configuration where the jet is laminar and the flow steady. Therefore surface tension, being the sole dominant force in this regime, keeps the free surface nearly flat preventing any air entrainment. It should be pointed out that this is a consequence of the smallness of the ratio μ/σ for water. According to the above analysis, for water, the required minimum jet velocity for laminar entrainment (so that $Ca > 1$) is around 70 m s^{-1}. However, this limit is impossible to reach in practice as the jet becomes turbulent at much lower velocities. As noted before, laminar jets of high viscosity that are not enclosed with a hollow cap are known to entrain air in the form of a thin film around the jet below the free surface for $Ca > 1$. See Lin & Donnelly (1966).

The conclusions from this simple dimensional analysis are consistent with observation. In figure 3(*a*) we show an image of the cap where a smooth laminar jet meets the cylindrical body of water in the cap. In this backlit picture, water appears bright and air dark. The jet issuing from left to right is visible in the dark air cavity on the left. In this case there is no air flow into the cap and there are no entrained bubbles. This configuration is quite stable in the absence of mechanical disturbances.

As air is supplied into the cap, the air shroud around the jet moves downstream (to the right in figure 3*b*) and extends all the way to the exit of the cap where large bubbles are seen to grow and detach from the end of the cap into the liquid (figure 3*b*). In this first regime, the jet is laminar and only large bubbles can be entrained. It is of little interest for the purpose of producing small bubbles.

The transition to the second regime is observed when the jet velocity is increased

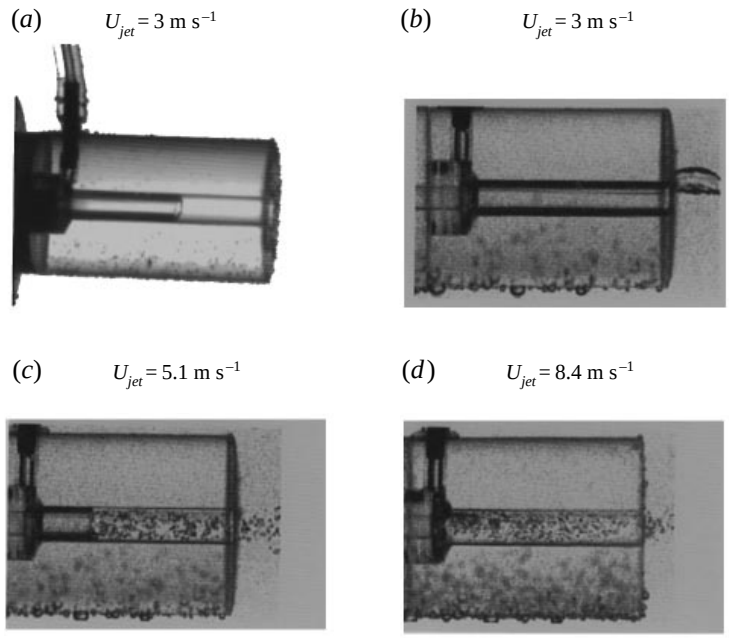

FIGURE 3. Three modes of nozzle operation: steady cavity shape for a smooth jet without entrainment (*a*). As the jet velocity is increased at a fixed airflow rate (0.278 ml s^{-1}) (*b*), the jet becomes rough and the air cavity in the cap shrinks (*c*, *d*).

to the point that its surface becomes rough. At this point the jet becomes turbulent and starts entraining small air bubbles into water. The jet entry point moves back (to the left in figure 3*c*) from the exit of the cap toward the nozzle exit. The process of air entrainment now occurs inside the cap (figure 3*c*) rather than at the exit as in figure 3(*b*). Entrained bubbles are seen as small black dots in this picture. The boundary between the regimes (*b*) and (*c*) is obviously a function of the cap's length as well as the flow conditions.

The inertial forces are drastically different in this second regime than the smooth jet case of the first regime. Disturbances riding on the jet surface are capable of creating an over-pressure of the order of ρU_{jet}^2 upon hitting the free surface. Assuming that the surface tension opposes this pressure force, a Weber number can be constructed as

$$We = \frac{\rho U_{jet}^2 \epsilon}{\sigma}, \tag{3}$$

where ϵ is the average amplitude of disturbances on the jet surface. If we take $\epsilon = 20$ μm, for instance, we find $We = 7$ for $U = 5$ m s^{-1} and $We = 4.6$ for $U = 4$ m s^{-1}. So it appears that the inertia of the little bumps on the jet surface is strong enough to deform the free surface and entrain bubbles even for disturbances as small as 20 μm. As for viscous effects, it is reasonable to assume that the role of viscosity on entrainment remains negligible since the relevant quantities such as U_{jet}, μ, σ, and δ are hardly affected by the unsteady nature of the flow when compared to the laminar jet case. Therefore, the previous analysis of the viscous forces still holds in spite of the more complicated nature of the flow.

There is an interesting connection between the process of air entrainment by a jet and the length of the cavity in the cap. It has been known for some time that the

air entrainment rate is related to jet surface roughness (McCarthy *et al.* 1970) by a relation that can be approximated by

$$Q_{ent} = 2\pi R_{jet}\epsilon(L)U_{jet}, \tag{4}$$

for disturbances that are small compared to the jet radius. Here $\epsilon(L)$ is the average jet roughness at a distance L from the nozzle exit. Since R_{jet} and U_{jet} are almost constant throughout the length of the cap, the range of ϵ, i.e. $\epsilon_{min} - \epsilon_{max}$, determines the range of the second regime in figure 3(*c*). If ϵ were almost uniform over the jet length, there would only be a narrow range of U_{jet} for which $Q_{ent} = Q_{air}$ where Q_{air} is the imposed air flow rate into the air shroud around the jet. Indeed, if U_{jet} were greater than the equilibrium value, more air than is supplied into the cap would be entrained and the air shroud would disappear as the turbulence level at the exit of the nozzle would be sufficient to instantly disintegrate air injected into the cap into small bubbles before they can form a continuous shroud around the jet (figure 3*d*). This third regime is similar to a Venturi type aeration commonly found in many industrial systems. Conversely, when U_{jet} is smaller than the critical value, less air will be consumed by the jet and the air shroud will grow out of the cap as in figure 3(*b*).

It is evident that, in order to have a broader range of stable entrainment, there must be a mechanism that increases the entrainment rate as the air cavity grows and decreases it when it contracts. Equation (4) shows that a disturbance level ϵ increasing with the jet length L exposed to air would have precisely this effect. This point can be demonstrated by means of a simple kinematic model constructed by using the conservation of air in the cavity. We first develop the model for the general unsteady process, and then study the time-independent solution. Assuming that the air density is constant, a mass balance gives

$$\pi(R_{cap}^2 - R_{jet}^2)\dot{L} = Q_{air} - Q_{ent} \tag{5}$$

where $\dot{L}$ is the time derivative of the cavity length, Q_{air} is the air flow rate injected into the cavity, and R_{cap} is the inner radius of the cap. Consider a case in which we have a roughness distribution described around the equilibrium position of the interface by

$$\epsilon(L) = \alpha + \beta L, \tag{6}$$

where α and β are constant. Since the capillary waves on the jet grow, one expects β to be positive as is indeed confirmed by our and others' experiments (see e.g. Van Dyke 1982, p. 105). When (4) and (6) are employed in (5) together with the condition $\dot{L} = 0$, the equilibrium length of the cavity, L_0, is obtained as

$$L_0 = \frac{Q_{air} - 2\pi R_{jet}U_{jet}\alpha}{2\pi R_{jet}U_{jet}\beta}. \tag{7}$$

Substitution of (4) and (6) into (5) yields the evolution equation for L

$$\pi(R_{cap}^2 - R_{jet}^2)\dot{L} + 2\pi R_{jet}U_{jet}\beta(L - L_0) = 0. \tag{8}$$

Hence L satisfies a relaxation relation with a time constant of

$$\tau = \frac{R_{cap}^2 - R_{jet}^2}{2R_{jet}U_{jet}\beta}. \tag{9}$$

When typical values are substituted into (9), the cavity response is found to be consistent with observation. For instance, the case in which $U_{jet} = 7$ m s^{-1}, $R_{cap} =$

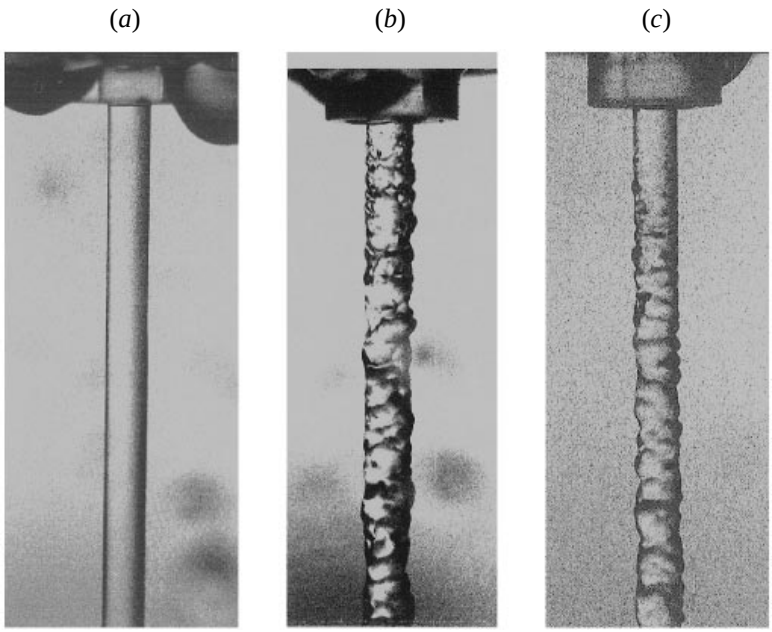

FIGURE 4. Jet shapes produced by smooth, sharp and conical nozzles. Here the jet velocity and radius are 7.3 m s^{-1} and 0.8 mm respectively.

1.2 mm, $R_{jet} = 0.8$ mm, $\beta = 10\ \mu m/5$ mm $= 0.0002$, yields a time constant of $\tau = 0.36$ s as compared with a value of 0.5 s estimated from the experiment. Note that according to (7), a stable L_0 cannot be attained if $\beta < 0$. It is also evident that an excessively small value of β would present problems. Indeed, it was very difficult to find an equilibrium position for jets with a nearly uniform roughness distribution, i.e. small β. In those cases, the cavity wildly oscillated back and forth in the cap.

To estimate the amplitude of fluctuations in L we consider the situation in which the jet roughness goes through a sudden change. If we assume that this jump is $\Delta\epsilon$ and its duration is Δt then the parameter α in (6) becomes

$$\alpha = \alpha_0 + \Delta\epsilon[H(t) - H(t - \Delta t)], \tag{10}$$

where α_0 is the equilibrium value and H is the Heaviside function. The response of the system is obtained by solving the differential equation (8),

$$L - L_0 = -\frac{\Delta\epsilon}{\beta}\left[\left(1 - e^{-t/\tau}\right) - H(t - \Delta t)\left(1 - e^{-(t-\Delta t)/\tau}\right)\right]. \tag{11}$$

For very short durations, i.e. $\Delta t \ll \tau$, the maximum deviation of the cavity from its previous position is $L_{max} - L_0 \approx \Delta\epsilon\Delta t/\beta\tau$. In this case, stability of the cavity can be maintained even if $\Delta\epsilon$ is relatively large. The excess air entrained during Δt shortens L only by an amount $2\pi R_{jet} U_{jet}\Delta\epsilon\Delta t/\pi(R_{cap}^2 - R_{jet}^2)$. In the other limit, for $\Delta t \gg \tau$ we have instead $L_{max} - L_0 \approx \Delta\epsilon/\beta$ that can be very large. In fact, we have observed cases in which the fluctuations in L spanned the entire length of the cap as mentioned before. The stability of the air cavity is important in terms of determining the operation range of the nozzle.

We have tried several types of nozzles to achieve a stable cavity. According to the above analysis, the requirement is that ϵ is a monotically increasing function of L with a slope, β, that is sufficiently large. Guided by the work of McCarthy & Molloy (1974)

Nozzle	d_c	d (mm)	l (mm)	α (deg.)	D (mm)	L (mm)
I	1.6	2.4	3.81	20	6.35	25.4
II	2.0	2.8	5.08	20	6.35	25.4
III	2.4	3.2	6.35	20	6.35	25.4

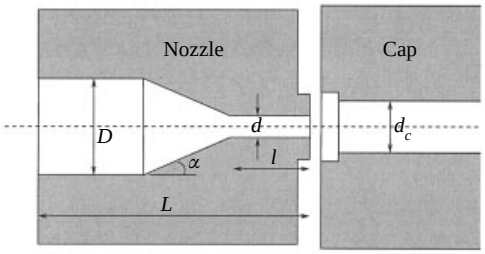

TABLE 1. Geometric description of the nozzles used in the experiments.

three basic nozzle types, smooth, conical, and sharp, have been constructed. The jets produced by these nozzles are shown in figure 4. The smooth nozzle has a cosine reduction profile and produces a very smooth jet even at relatively high velocities up to 8 m s^{-1}. The second type of nozzle has a sharp step-like reduction which produces substantial turbulence right at the exit. The amplitude of the disturbances does not seem to change very much as a function of the distance from the jet exit over the distances of interest here. As a consequence, no stable equilibrium position can be found for the first and second type nozzles. Typically, the air cavity moves back and forth in the entire span of the cap at a freqeuncy of about 1 Hz. This behaviour is completely consistent with the simple analysis presented above. The conical nozzle is basically a truncated cone with a half-opening angle of 20°. The jets produced by this nozzle seem to be suitable for our purposes. Based on the above observations, the conical nozzle seems to be a suitable choice for studying the air entrainment process. All the subsequent experimental results are obtained with conical nozzles (third type). In the next section we study in detail surface properties of jets generated by these nozzles.

4. Jet surface roughness

We have used three nozzles of conical cross-section with radii 0.8, 1.0 and 1.2 mm. The geometric parameters of these nozzles, machined from aluminum, are given in table 1.

For a better observation of the surface roughness the camera was positioned close to the jet. As a consequence the field of view was small and only 5 mm axial sections of the jet could be acquired at the maximum magnification, at which the resolution was 7.3 μm per pixel along the axial direction and 8.4 μm per pixel radially. Four sections were imaged in the range 0 to 20 mm with 5 mm increments. The jet profiles were extracted from the online images by using a simple thresholding technique. The online data collection was chosen in favour of processing pre-recorded images in view of the enormous storage capacity required for several thousand pictures. Typical examples are shown in figure 5. For each section of the jet, 50 images were captured at about 1 s intervals. In order to account for a possible azimuthal non-uniformity the process was repeated for jets rotated 90° around their axis. In this way, a total of 200 profiles for each axial section were recorded for further processing.

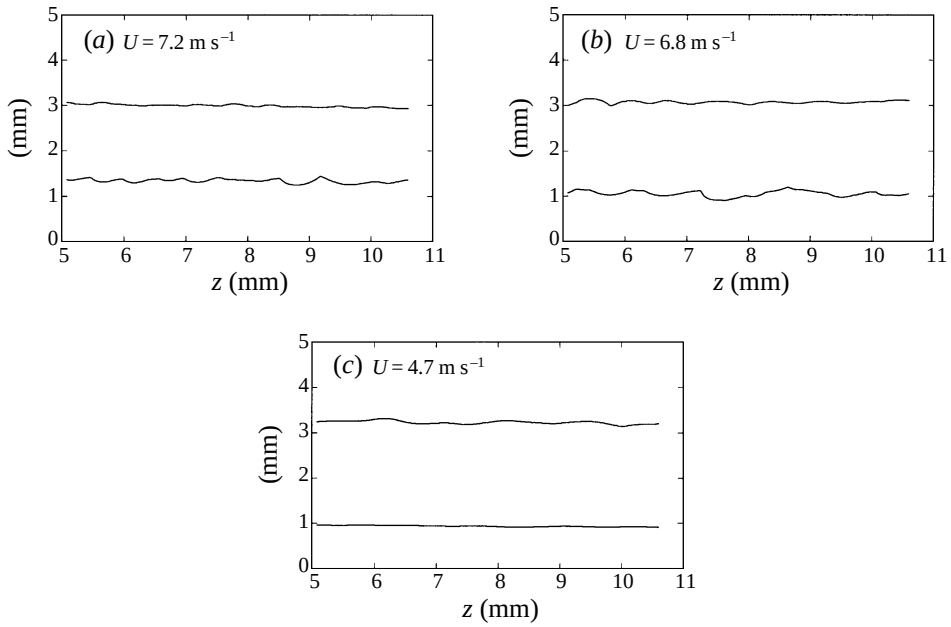

FIGURE 5. Typical jet profiles obtained from CCD images of the (5–10 mm) axial section of the jet. The coordinate z is measured from the nozzle exit. (*a*) $R = 0.8$ mm, (*b*) $R = 1$ mm, (*c*) $R = 1.2$ mm.

To quantify the variation of the jet surface roughness as a function of the distance from the nozzle exit z, we define the roughness $\epsilon(z)$ as the average of the r.m.s. average over a distance Δ of 1 mm around z. For each jet profile there are two edges, one on each side of the image. Suppose that one of the edges of the jth profile is defined by the coordinates $(r^{(j)}, z)$. Then we define

$$\epsilon^{(j)}(z) = \left(\frac{1}{2\Delta} \int_{z-\Delta}^{z+\Delta} (r^{(j)} - \bar{r})^2 \right)^{1/2} \mathrm{d}z$$

where

$$\bar{r}(z) = \frac{1}{2\Delta} \int_{z-\Delta}^{z-\Delta} r^{(j)} \mathrm{d}z.$$

The ensemble average of this quantity at a fixed z gives

$$\epsilon(z) = \frac{1}{N} \sum_{j=1}^{N} \epsilon^{(j)}(z) \tag{12}$$

where $N/2$ is the total number of images or profiles for a given section.

In figure 6(*a–c*) we show $\epsilon(z)$ for various jet speeds and radii. As evident from figure 4, ϵ is small at the jet exit but increases gradually further downstream from the exit. In all the cases presented here the roughness was too small to be detected by our CCD camera in the range $z = 0$–0.5 mm. From $z = 0.5$ mm onward, $\epsilon(z)$ shows a rapid increase but levels off at some distance from the exit.

To establish a connection between ϵ and the air entrainment rate we measured the length of the air cavity, i.e. the distance from the jet exit to the intersection point where the jet hits the body of water in the cap (see figure 3). The air entrainment rate is simply deduced from the measured air flow rate (figure 2) under the assumed

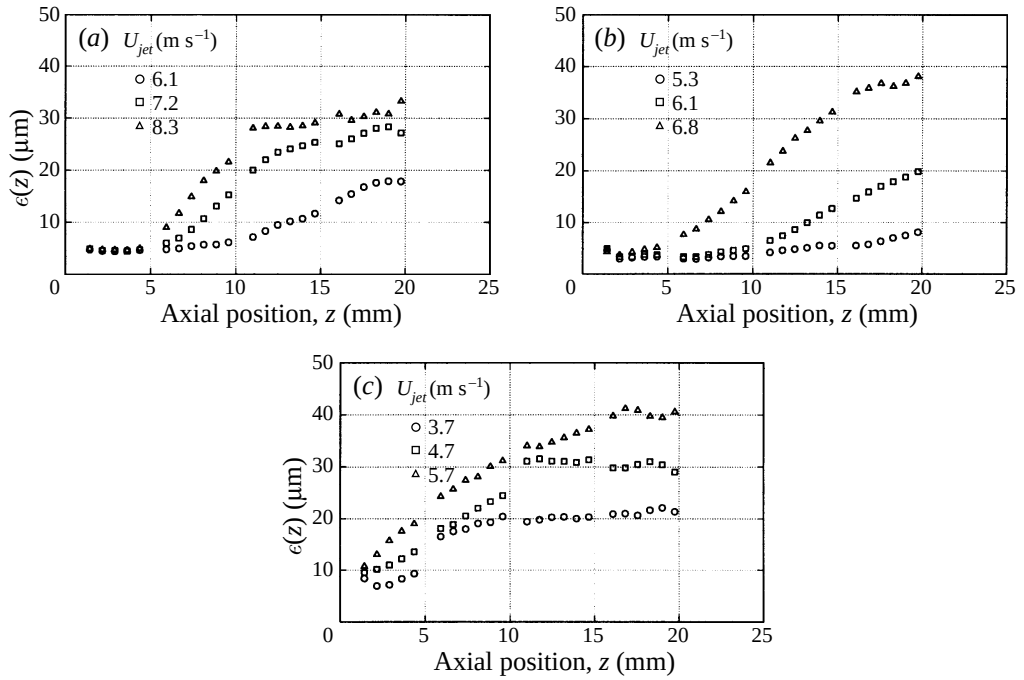

FIGURE 6. Graph of the axial dependence of jet surface roughness for three nozzles at various flow rates. (*a*) $R = 0.8$ mm, (*b*) $R = 1$ mm, (*c*) $R = 1.2$ mm.

steady-state conditions ($Q_{ent} = Q_{air}$). By using the air entrainment rate given by (4) we can also predict Q_{ent} from the knowledge of $\epsilon(L)$ as computed in (12). Since a positive β is required for stability, it is apparent from figure (6*a–c*) that there is a finite range of air entrainment rates for which a stable air cavity can be maintained in the cap at a fixed jet velocity. Even in this stable range, the intersection point was not always steady but fluctuated around the equilibrium position. The amplitude of these oscillations was usually small (of order 1 mm) except for cases corresponding to long cavities where it could be as high as 5 mm. A sequence of about 20 CCD images were acquired to obtain a mean value. In figure 7(*a–c*) we have plotted the measured entrainment rate as a function of the length of the air cavity in the cap together with the predicted rate given by (4). In all cases the two curves show a similar trend and in some they are on top of each other. The agreement is better for smaller nozzles and at higher speeds. The standard deviation of the r.m.s. averages, which can be interpreted as a measure of the roughness distribution in time at a fixed axial location, is also plotted in the same figure. The discrepancy between the measurements and (4) in figure 7(*c*) seems to be caused by the non-uniform distribution of the jet roughness. The validity of (4) for the cases considered in this study is however supported by these plots and the direct relationship between the air entrainment rate and the jet surface roughness is confirmed.

A close examination of the jet surface reveals that a train of waves become visible at around 5 mm from the jet exit and evolves into a complex shape further downstream. The average wavelength of these waves is computed by taking the fast Fourier transform of the profiles. A von Hann filter is used to first smooth out the edges of the jet profile and zero padding is supplied to extend the transform to 1024 points. The average power spectra obtained from these FFTs are plotted for successive 5 mm

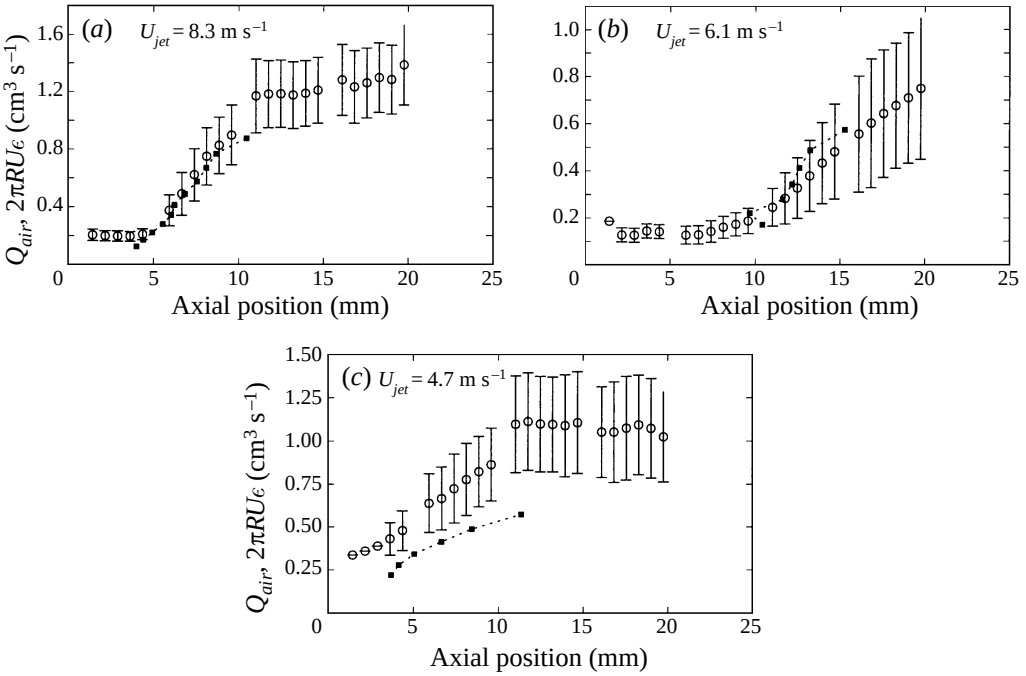

FIGURE 7. Measured (squares) and predicted (open circles) air entrainment rates as a function of the cavity length. The error bars represent the standard deviation of the r.m.s. roughness obtained from 200 measurements. (*a*) $R = 0.8$ mm, (*b*) $R = 1$ mm, (*c*) $R = 1.2$ mm.

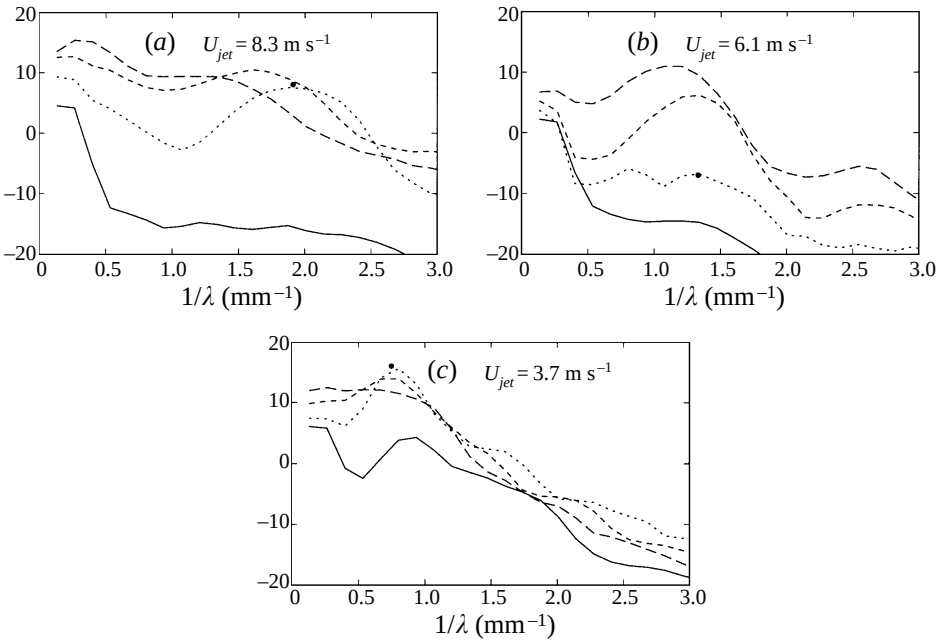

FIGURE 8. Power spectrum of jet surface profiles in the 5 mm sections from 0 to 20 mm from the jet exit. Section (0–5 mm) solid line, (5–10 mm) dotted line, (10–15 mm) dashed line, (15–20 mm) long dashed line. (*a*) $R = 0.8$ mm, (*b*) $R = 1$ mm, (*c*) $R = 1.2$ mm.

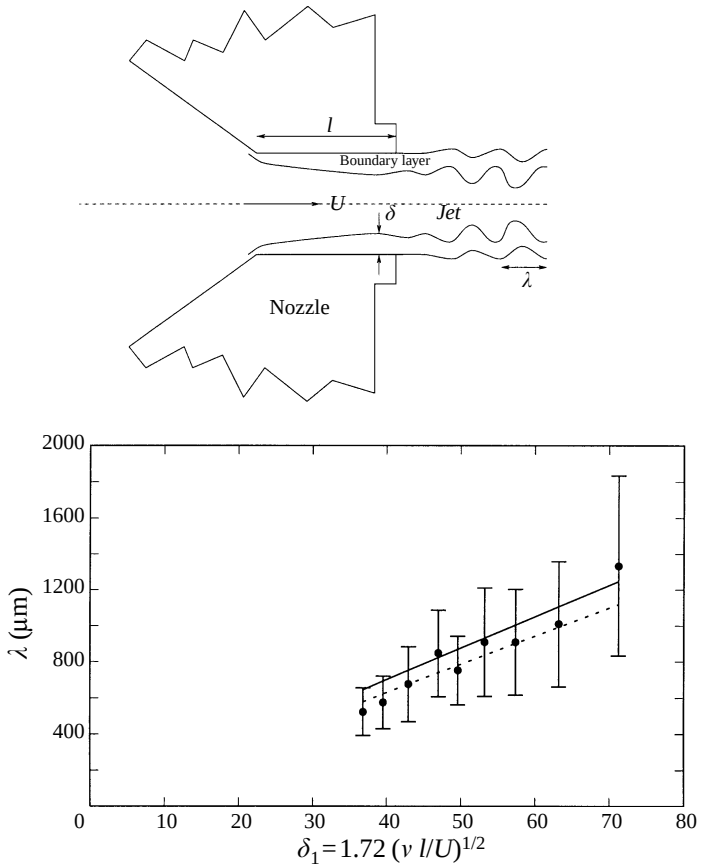

FIGURE 9. Proposed mechanism of the formation of jet surface roughness and the graph of the average wavelength as a function of the momentum thickness. The solid and dashed lines represent the equations $\lambda = 17.5\delta_1$ and $\lambda = 15.7\delta_1$ which were developed for a boundary layer on a flat plate.

sections of the jet in figure 8(*a–c*). The first peak appearing in these plots at $1/\lambda = 0.2$ mm^{-1} corresponds to the length of the trace (5 mm). The second peak, which is more pronounced in the 0.8 and 1.0 mm nozzles, is due to the waves on the jet surface. The identification of the average wavelength is done by inspecting the average power spectrum of the second 5 mm section (i.e. in the interval 5–10 mm) of the jet where waves seem to appear first.

To explain the origin of these waves and derive an expression for the wavelength in terms of flow conditions, we assume that the boundary layer that develops inside the nozzle becomes unstable and causes roughness on the jet surface. A similar mechanism has been proposed by Dai, Hsiang & Faeth (1996) for a coaxial free jet where the onset of the free surface roughness has been correlated to the instability of the boundary layer. It must be noted that we are dealing with jets that are in the transition regime from laminar to turbulent. By using the well-known theory of Tollmien–Schlichting waves we can relate the momentum thickness to the wavelength λ. For simplicity, curvature effects can be ignored in our case in view of the short exit section of the nozzles which keeps the boundary layer thin with respect to the jet radius. According to the Blasius boundary layer stability analysis (Schlichting 1979)

we have the lowest unstable wavelength at the onset given by

$$\lambda = C\delta_1 \tag{13}$$

where δ_1 is the displacement thickness and C is a constant given as 17.5 by Schlichting (1979) which is slightly higher than its experimental value 15.7 (Drazin & Reid 1981). Although more refined procedures for predicting the instability point have been developed over the years, (13) is adequate for the purpose of establishing a connection between the jet surface roughness and the boundary layer. For a current review of boundary layer stability see Reed, Saric & Arnal (1996). Here δ_1 has the usual value

$$\delta_1 = 1.72(\nu l/U_{jet})^{1/2} \tag{14}$$

and l is the distance from the leading edge. In our case we may set this quantity to the length of the straight exit section of the nozzle. In figure 9 we plot λ obtained from the power spectra of the surface as a function of δ_1 together with (13) with $C = 17.5$ and $C = 15.7$. The agreement between the measurements and (13) is remarkable in spite of the obvious difference in the geometry of the problems. It is evident from this plot that a relationship between these quantities exists, supporting the hypothesis put forward above.

5. Bubble size measurements

Bubble size measurements were carried out in an automated manner from online images acquired during the experiments. An elaborate procedure was developed to eliminate errors commonly associated with this process. Various steps of the algorithm are depicted in figure 10 for two images taken at 0 cm from the cap exit where there are many bubbles and at 3 cm where bubbles are scarce but large. The images are first passed through an edge detection algorithm followed by a threshold filter. The resulting black and white image contains only the sharp edges of the original image (figure 10ii). This procedure eliminates off-focus bubbles. We have not attempted to extract useful information from bubbles outside the focal plane which is centred around the jet axis. Individual bubble shapes are searched by scanning this image and the bubble boundaries are computed as a stream of x and y values by tracing the transition from black to white. The boundary of each bubble is then passed through a curvature test to eliminate overlapping bubbles. A very high curvature along the boundary relative to the average radius is assumed to signify that the detected shape contains more than one bubble. Examples of this situation can be found in figures 10(a)(iii) and 10(b)(iii) where the algorithm correctly eliminates the shapes of overlapping bubbles. Once a bubble shape passes these tests, its area is computed in terms of the number of pixels. The bubble radius is computed as the equivalent radius of a circle. As explained in § 2, a resolution of 7.2 μm horizontally and 8.4 μm vertically is achieved in these measurements. This limits the smallest detectable bubble size to about 10 μm.

For each case reported in this paper we acquired around 100 images and measured on the average 2000 bubbles. Typical bubble size distributions are shown in figure 11 corresponding to nozzles of different sizes. The measurements denoted by solid, dotted and dashed lines are made at 0, 1 and 3 cm from the exit of the cap respectively. The axial width of each image is 5 mm. As evident from the plots the size distribution becomes wider for larger nozzles. At the same time we note that the power spectra in figure 8 exhibit multiple peaks for larger nozzles. This observation suggests a

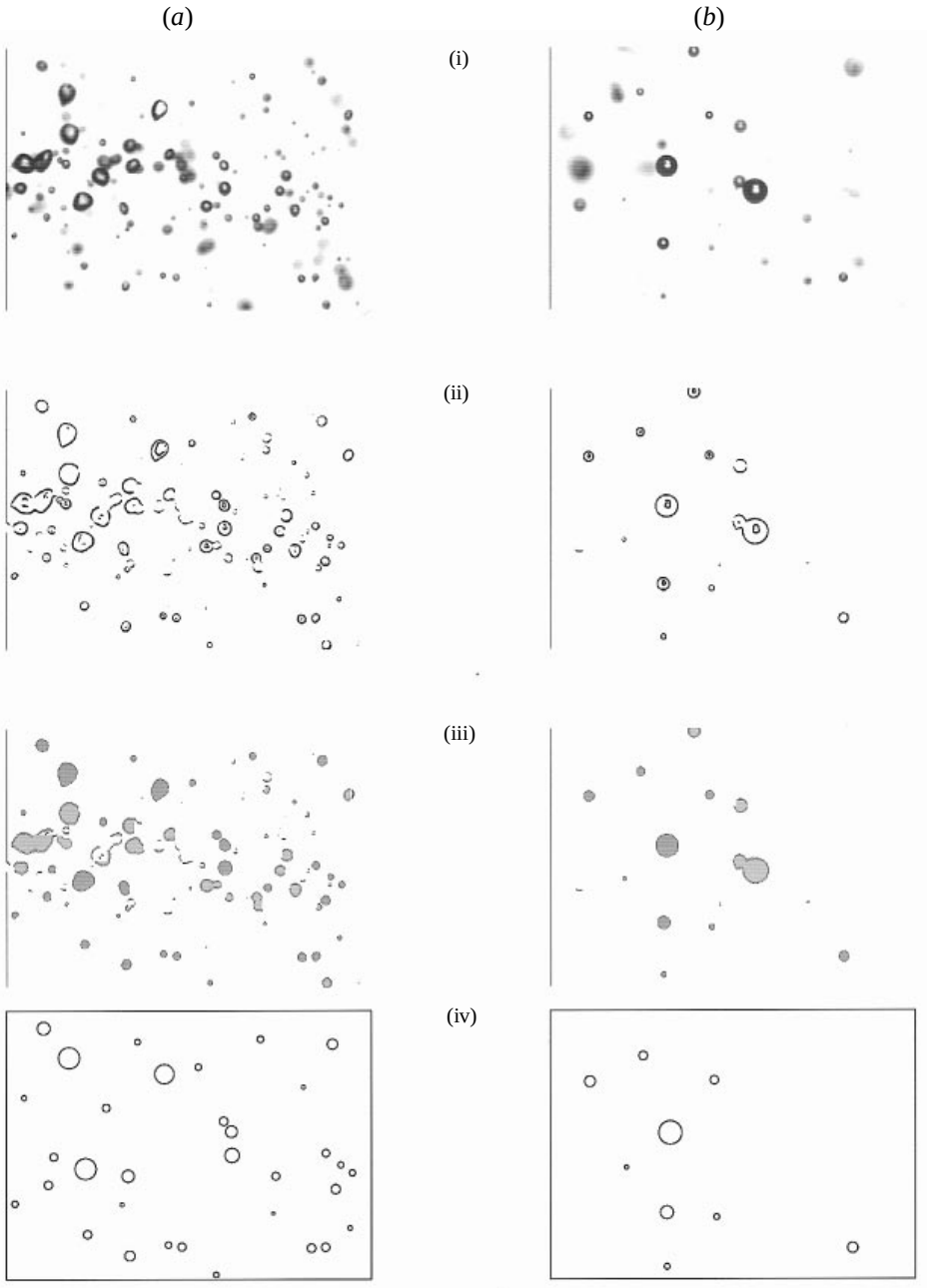

FIGURE 10. Two sequences of images at 0 and 3 cm from the cap exit showing different steps involved in the algorithm for measuring bubble sizes from acquired pictures.

relationship between the wavelength of the surface disturbances and the bubble size, which will be explored further in this section.

In all three cases, a widening of the distribution, although to a lesser to degree, is also observed as the measurement location is moved away from the cap. There are basically two factors responsible for this shift towards larger bubbles. The first one is

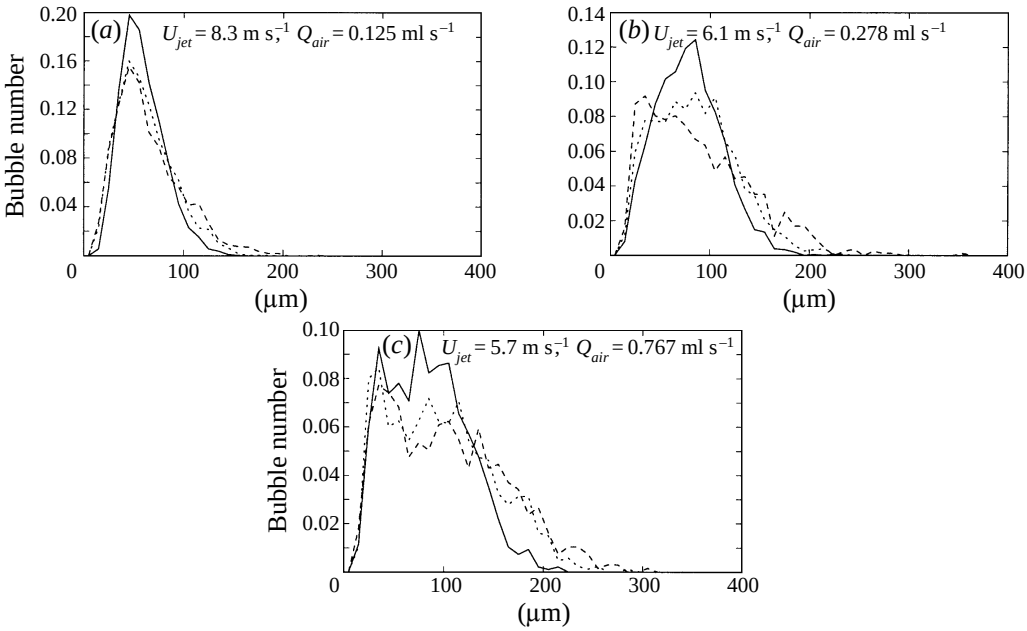

FIGURE 11. Normalized bubble size distribution for different nozzles at 0 (solid line), 1 (dotted) and 3 (dashed) cm from the cap exit. $r = 0.8$ mm, $r = 1$ mm, $r = 1.2$ mm.

due to the difference in the bubble velocities. Since large bubbles slow down faster than small bubbles, they appear more abundant further downstream. This trend continues up to a certain critical point beyond which they completely disappear, partly due to the buoyancy force. Further downstream, only smaller bubbles can be seen. The measurement locations were much nearer to the cap exit than this critical point. Therefore the velocity effect is observed as a shift towards larger bubbles in the present measurements. The second factor is coalescence, which is expected to occur at high void fractions in the bubble mixture.

The change in the bubble sizes is quantified by plotting the average radius of the distribution at 0 and 3 cm in figure 12(*a*) as a function of the flow ratio Q_{air}/Q_{water}. First we note here that the range is confined between 50 and 100 μm which is difficult to achieve with conventional techniques, e.g. using a porous surface. An average bubble radius of 50 μm is considered desirable in an actual implementation (de Rijk, van der Graaf & den Blanken 1994). However, the average bubble size increases substantially further downstream. The percent change between the 0 and 3 cm measurements is plotted in figure 12(*b*). There is some scatter in the data but there seems to be a linear increase with the flow ratio. Since this difference is due to both velocity and coalescence effects, the question of the role of coalescence cannot be resolved by these plots. To address this point we consider the maximum bubble radius which can be a good measure of the effect of coalescence in spite of it being prone to statistical errors. In figure 13(*a*) the maximum bubble radii at 0 and 3 cm are plotted as a function of the flow ratio. The fact that the maximum radius changes as a function of distance is already an indication of coalescence. However, this change, which is plotted separately in figure 13(*b*) as a percentage, is found to be insensitive to the flow ratio.

We have discovered an interesting connection between the average wavelength of

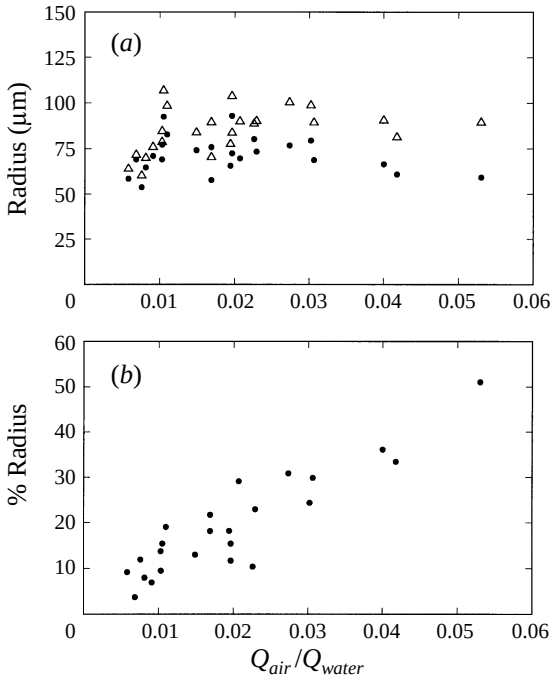

FIGURE 12. Average bubble size at 0 (solid circles), 3 (open triangles) cm from the cap exit as a function of the flow ratio Q_{air}/Q_{jet} (*a*). The percent change from 0 to 3 cm is plotted in (*b*).

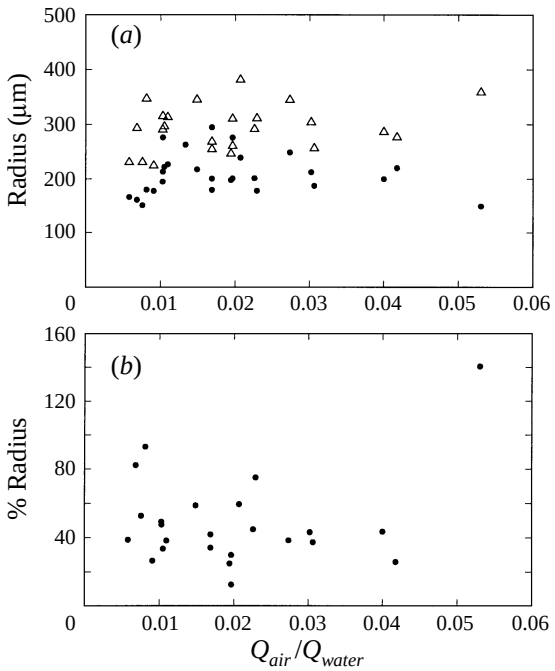

FIGURE 13. Maximum bubble radius at 0 (solid circles) and 5 (open triangles) cm from the cap exit as a function of the flow ratio Q_{air}/Q_{jet} (*a*). The percent change from 0 to 3 cm is plotted in (*b*).

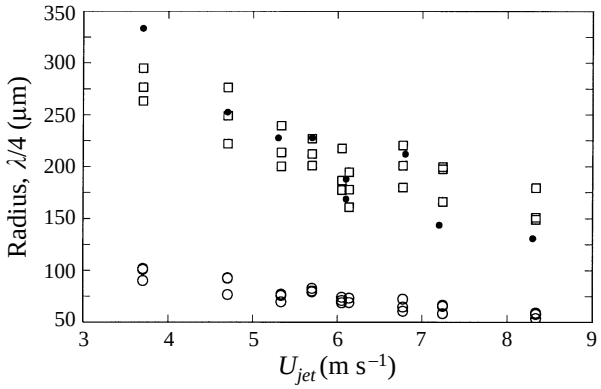

FIGURE 14. Average (open circles) and maximum bubble radii (open squares) and the quarter wavelength of the jet surface waves (solid circles) as a function of the average jet velocity.

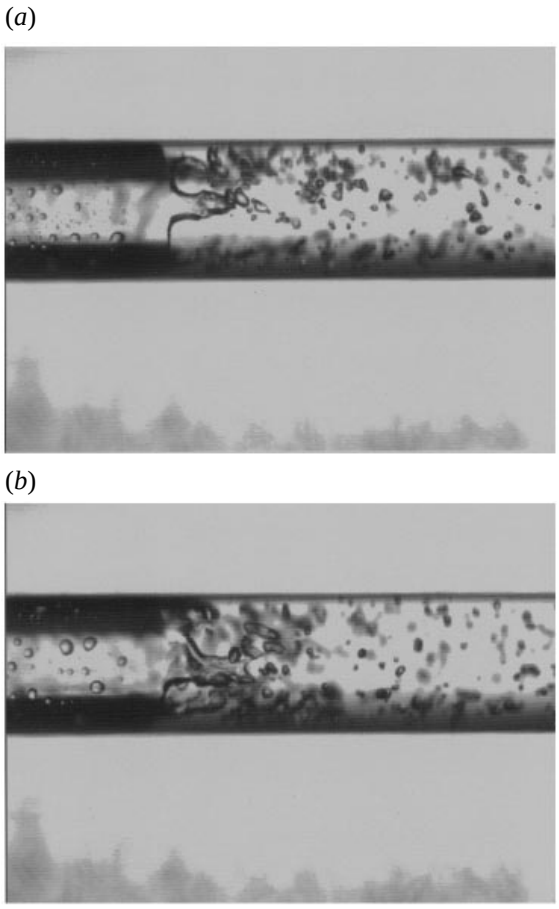

FIGURE 15. Close up images of the bubble formation in the cap. Here the jet radius and the cap's inner radius are 0.8 and 1.2 mm respectively.

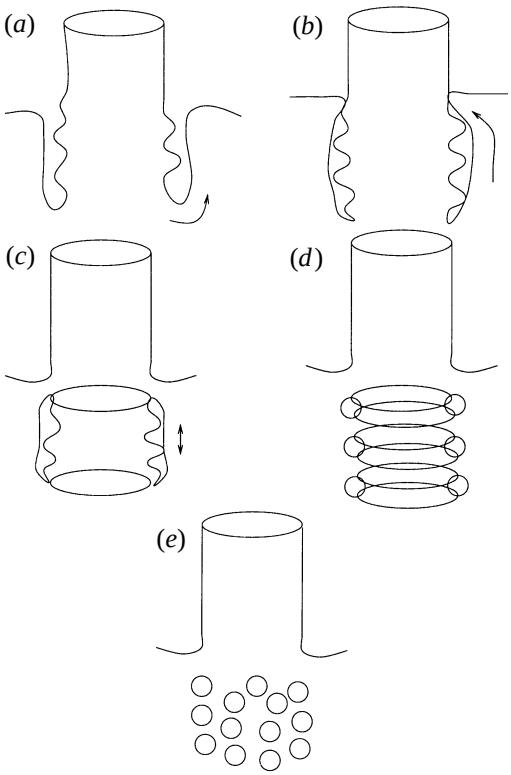

FIGURE 16. Proposed mechanism of bubble formation by the jet. Axial symmetry is assumed for clarity.

the jet surface waves and the maximum bubble size. In figure 14 a plot of these quantities basically implies that the maximum bubble radius is around $\lambda/4$ over the range of the cases covered here. Although we do not have conclusive evidence of the actual mechanism responsible for this relation we propose the following explanation based on the available experimental evidence. From closeup images such as the ones shown in figure 15 it is evident that the bubbles are mostly formed by the breakup of much larger cavities or pockets around the jet. An idealization of the process is depicted in figure 16 where for clarity we assume axial symmetry although this is not necessary. Large cavities are initiated by disturbances on the jet surface and penetrate up to 1 mm into the liquid before disintegrating into smaller bubbles. Assuming that the thickness of the cavity is comparable to the roughness amplitude ϵ we expect the depth and width of the cavity to be much greater than its thickness. When the cavity is closed off at the top it breaks up into smaller bubbles. The dominant length scale of the breakup in the axial direction is governed by the jet surface properties. In this direction, the diameter of the newly formed annular bubbles should be comparable to the half-wavelength of the jet roughness. If the breakup of the bubbles along the perimeter of the jet follows the axial breakup, the average bubble diameter is expected to be of the same order as the annular bubble diameter. Bubbles produced in this way are further broken up by the turbulence generated by the jet. Therefore it is reasonable to assume that the size of the largest bubbles is correlated to the wavelength of the jet surface roughness (figure 14).

6. Numerical simulations

The experimental observations on bubble generation can be put in a theoretical context by focusing on the formation of the air pockets shown in the images of figure 15. The region of interest is then the annular section around the jet inside the cap. We are interested in forces causing the deformation of the free surface of this region near the jet.

In the absence of any analytical solutions describing this process we turn to numerical simulations to study its dynamics. Unfortunately, numerical simulation of the full problem is very difficult and a number of simplifications are necessary. Following Prosperetti & Oguz (1997) viscous effects are ignored and a boundary integral code is utilized to simulate the free surface deformation. The numerical model involves a number of idealizations such as the inviscid flow assumption and axial symmetry. Nevertheless, these simulations are quite useful in identifying certain crucial factors. The velocity field is represented by a potential ϕ which obeys $\nabla^2\phi = 0$ as demanded by the continuity equation.

The code simulates the liquid motion in the annular region between the jet and the cap's inner wall. The numerical domain of the simulations is a rectangle in the meridian plane of the jet defined in cylindrical coordinates by $R_{jet} < r < R_{cap}$ and $0 < z < Z_{max}$. The equilibrium free-surface location corresponds to $z = 0$ and Z_{max} is large enough that end effects can be ignored. A value of $4(R_{cap} - R_{jet})$ is used in the simulations. Three sides of the numerical domain defined by $r = R_{jet}$, $r = R_{cap}$ and $z = Z_{max}$ are assumed to be impermeable, i.e. the normal derivative of ϕ is zero. The free surface at $z = 0$ is assumed to be flat initially.

The actual bubble generation event is simplified as follows. A pressure pulse of $\rho U_{jet}^2/2$ over a ring around the jet is used to mimic the effect of the disturbances. This is based on the concept that, when a bump riding on the jet hits a stationary free surface it generates a stagnation pressure of approximately $\rho U_{jet}^2/2$. In this scheme, the force exerted by this bump is taken into account while its mass is ignored. The width of the ring is set to a value comparable to the roughness of the jet. The only opposing force to the penetration of the pressure pulse is surface tension. A force balance gives the critical Weber number of (3) $We_{crit} = 2$.

Initially, ϕ is zero on the free surface, which is flat so that the fluid is stagnant. The evolution of ϕ on the surface is given by the Bernoulli integral

$$\frac{\mathrm{D}\phi}{\mathrm{D}t} = \tfrac{1}{2}|\nabla\phi|^2 + \frac{\sigma}{\rho}\mathscr{C} + P(r) \tag{15}$$

where $\mathscr{C}$ is the curvature, and $P(r)$ is non-zero and equal to $\rho U_{jet}^2/2$ only in the narrow region $(r - R_{jet}) < \epsilon$.

In figure 17 we show free-surface shapes at different times given in units of 0.1 ms at the upper left corner of each frame for a jet of $R = 0.8$ mm, $U = 6$ m s^{-1} and $\epsilon = 20\,\mu$m. The jet is shown at the left of each frame and is assumed to be straight. The computational domain is the shaded region in these plots. The annular cavity deforms as a result of the applied pressure pulse and a very narrow cavity around the jet is formed. In this case $We = 10.2$ which is above We_{crit}. The penetration of the cavity therefore proceeds unimpeded. Similar shapes are obtained in simulations with higher values of We. The cavity length in the last frame is 1.6 mm which is consistent with observations (figure 15). Capillary waves are initiated as a result of this deformation and propagate towards the cap's inner wall. They are then reflected back towards the jet entrapping a pocket of air. As expected, this tendency to close is

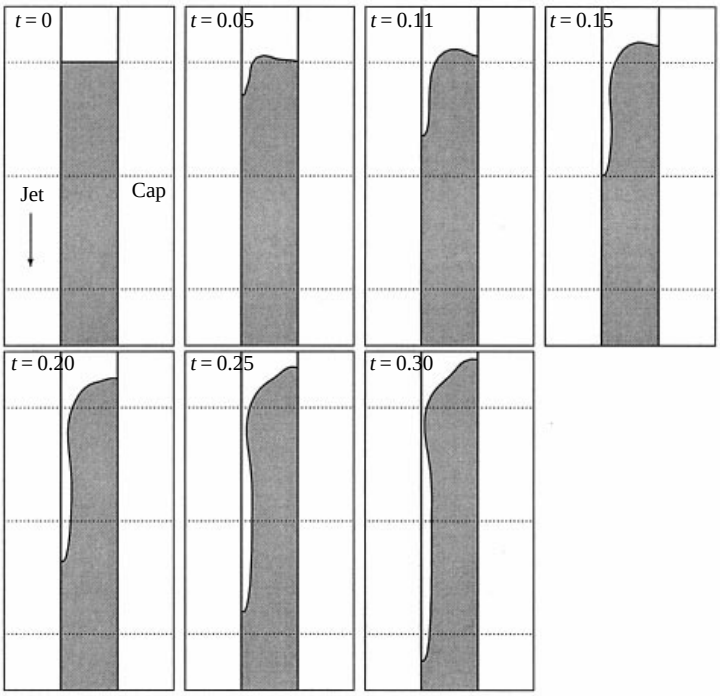

FIGURE 17. Boundary integral simulation of cavity formation by a disturbance on a jet. The effect of the disturbance is approximated by a ring of width ϵ over which an overpressure of $\rho U^2/2$ is applied. Here $We = \rho U^2 \epsilon/\sigma = 10.3$ and the cavity advances indefinitely into the liquid. The case corresponds to $U = 6$ m s^{-1}, $\epsilon = 20\,\mu$m, $R = 0.8$ mm and $R_{cap} = 1.2$ mm. Times are given in 0.1 ms.

inhibited at higher Weber numbers (not shown here). The time scale for this process is given by the total travel distance which is equal to twice the width of the annular region D, divided by the velocity of the capillary waves

$$\Delta t_c = \frac{2D}{(2\pi\sigma/\rho\epsilon)^{1/2}}. \tag{16}$$

For the case in figure 17 Δt_c is around 0.17 ms which is higher but of the same order of magnitude as the simulation value of 0.03. It must be noted that the wave reflection, which is not a factor in the case of an unbounded domain, prevents the cavity from becoming too large. In reality, the cavity close-off is probably controlled more by the incoming bumps on the jet surface. Jet profiles also suggest that these bumps are not isolated but appear in the form of a wave train, increasing the possibility of cavity closure.

When ϵ is set to half of its value in the previous case ($We = 5.1$) cavity penetration is significantly inhibited (figure 18). Initially, the free surface deforms much in the same way as in figure 17 but the process decelerates after a certain time when the curvature becomes large near the jet. These simulations agree with the case presented in figures 6(b) and 7(b) where the onset of the entrainment is observed around $U = 6$ m s^{-1} and $\epsilon = 10$ μm. Threshold points extracted from all measurements are plotted in figure 19 in the form of a critical We below which air entrainment is not possible. There is some scatter in the data due to the unstable nature of the cavity.

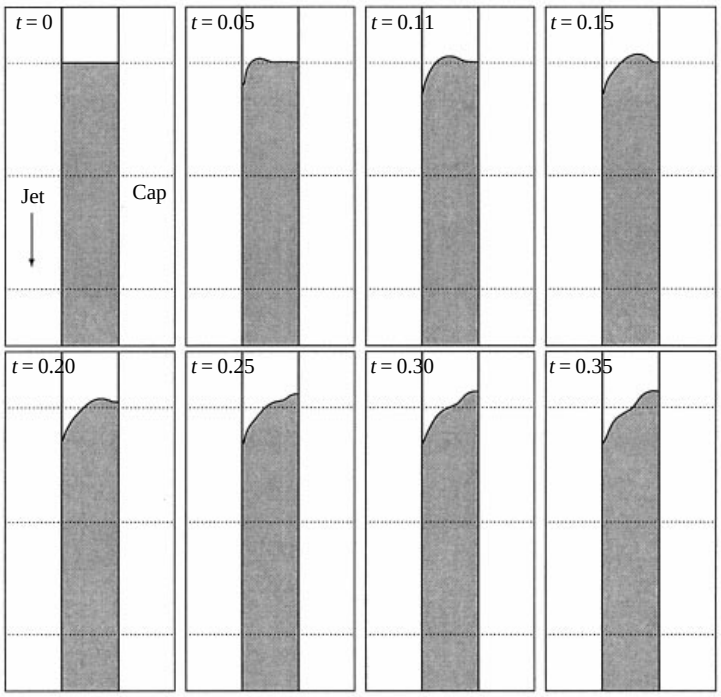

FIGURE 18. As figure 17 but here $\epsilon = 10\,\mu\text{m}$, $We = \rho U^2 \epsilon/\sigma = 5.2$ and the cavity tends to stop at some distance.

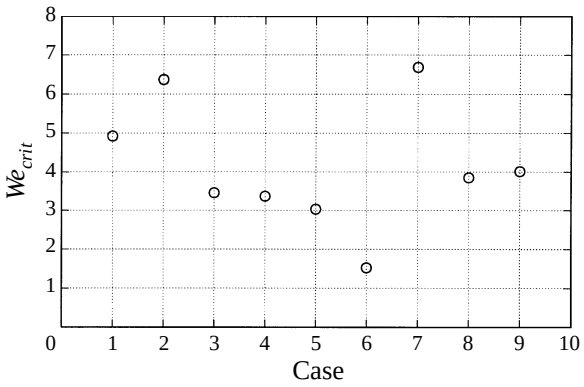

FIGURE 19. Graph of the critical Weber number above which entrainment is observed for cases covered in this study.

Nevertheless the critical Weber number seems to have an average value of 4 which is in approximate agreement with the simulations.

7. Conclusion

Bubble production by a liquid in a special nozzle has been studied experimentally and numerically. The results show the importance of the jet surface properties. This is in contrast to previous investigations which relied on non-dimensional numbers based on the jet itself. In particular, the average roughness of the jet is shown to control

the air entrainment rate and the average wavelength of the disturbances seems to be correlated to the bubble size distribution.

The nozzle geometry, which in turn defines the boundary layer structure in the jet, has a direct influence on the jet surface. Stable entrainment was achieved by using a conical nozzle that produces a jet with a monotonically increasing roughness.

It is found that bubble production is a result of the breakup of relatively large pockets of air that form around the jet. Numerical simulations are used to study the dynamics of formation of these pockets. Surface shapes obtained numerically are in general agreement with experiment. Based on the simulations and experimental observations, we concluded that surface tension is the limiting factor on the initiation of the air entrainment.

The author would like to thank Professor A. Prosperetti for his comments and suggestions during the course of this research, J. Libertini for her assistance in running the experiments and Professor J. Katz for some helpful comments. This study has been supported by the National Science Foundation grant no. CTS 9318724.

REFERENCES

Baker, C. T. & de Nevers, N. 1984 Bubble formation at vibrated orifices: medium-chamber-volume region. *AIChE J.* **30**, 37–44.

Bin, A. K. 1993 Gas entrainment by plunging liquid jets. *Chem. Engng Sci.* **21**, 3585–3630.

Blanchard, D. C. & Syzdek, L. D. 1997 Production of air bubbles of a specified size. *Chem. Engng Sci.* **32**, 1109–1112.

Boulton-Stone, J. M. & Blake, J. R. 1993 Gas bubbles bursting at a fine surface. *J. Fluid Mech*, **254**, 437–466.

Burgess, J. M., Molloy, N. A. & McCarthy, M. J. 1972 A note on the plunging liquid jet reactor. *Chem. Engng Sci.* **27**, 442–445.

Cunningham, R. G. 1974 Gas compression with the liquid jet pump. *J. Fluids Engng* **3**, 203–226.

Dai, Z., Hsiang, L.-P. & Faeth, G. 1996 Spray formation at the free surface of turbulent bow sheets. In *Proceedings of Naval Hydrodynamics, June 24–26, Norway*, pp. 197–211.

Detsch, R. M. & Sharma, R. N. 1990 The critical angle for gas bubble entrainment by plunging liquid jets. *Chem. Engng J.* **44**, 157–166.

Dixon, K. L., Lee, R. G., Smith, J. & Zielinski, P. 1991 Evaluating aeration technology for radon removal. *J. Am. Water Works. Assoc.* **83**, 141–148.

Drazin, P. G. & Reid, W. H. 1981 *Hydrodynamic Stability*. Cambridge University Press.

Lara, P. 1979 Onset of air entrainment for a water jet impinging vertically on a water surface. *Chem. Engng Sci.* **34**, 1164–1165.

Lin, T. J. & Donnelly, H. G. 1966 Gas bubble entrainment by plunging laminar liquid jets. *AIChE J.* **12**, 563–571.

Marmur, A. & Rubin, E. 1976 A theoretical model for bubble formation at an orifice submerged in an inviscid liquid. *Chem. Engng Sci.* **31**, 453–463.

McCarthy, M. J., Henderson, J. & Molloy, N. A. 1970 Entrainment by plunging jets. In *Proc. Chemeca 1970 Conf.*, pp. 86–100. Australia, Butterworths.

McCarthy, M. J. & Molloy, N. A. 1974 Review of stability of liquid jets and influence of nozzle design. *Chem. Engng J.* **7**, 1–20.

McKeogh, E. J. & Ervine, D. A. 1981 Air entrainment rate and diffusion pattern of plunging liquid jets. *Chem. Engng Sci.* **36**, 1161–1172.

Ohkawa, A., Kusabiraki, D., Kawai, Y. & Sakai, N. 1986 Sone flow characteristics of a vertical liquid jet system having downcomers. *Chem. Engng Sci.* **41**, 2347–2361.

Pamperin, O. & Rath, H. 1995 Influence of buoyancy on bubble formation at submerged orifices. *Chem. Engng Sci.* **50**, 3009–3024.

Prosperetti, A. & Oguz, H. N. 1997 Air entrainment upon liquid impact. *Phil. Trans. R. Soc. Lond.* A **355**, 491–506.

Ramakrishnan, S., Kumar, R. & Kuloor, N. R. 1969 Studies in bubble formation-i bubble formation under constant flow conditions. *Chem. Engng Sci.* **24**, 731–747.

Reed, H. L., Saric, W. S. & Arnal, D. 1996 Linear stability theory applied to boundary layers. *Ann. Rev. Fluid Mech.* **28**, 389–428.

de Rijk, S. E., van der Graaf, J. H. J. M. & den Blanken, J. G. 1994 Bubble size in flotation thickening. *Wat. Res.* **28**, 465–473.

Satyanarayan, A., Kumar, R. & Kuloor, N. R. 1969 Studies in bubble formation-ii bubble formation under constant pressure conditions. *Chem. Engng Sci.* **24**, 747–761.

Schlichting, H. 1979 *Boundary-Layer Theory*. McGraw-Hill.

Sene, K. J. 1988 Air entrainment by plunging jets. *Chem. Engng Sci.* **43**, 2615–2623.

Shah, Y. T. 1992 Design parameters for mechanically agitated reactors. *Adv. Chem. Engng* **17**, 1–206.

Tchobanoglous, G. & Burton, F. L. 1991 *Wastewater Engineering, Treatment, Disposal and Reuse*, 3rd Edn. McGraw-Hill.

Tsuge, H., Hibino, S. I. & Nojima, Y. 1981 Volume of a bubble formed at a single submerged orifice in flowing liquid. *Intl Chem. Engng* **21**, 630–636.

Tucker, C. S. & Robinson, E. H. 1990 *Channel Catfish Farming Handbook*. Van Nostrand Reinhold.

Van de Sande, E. & Smith, J. M. 1973 Surface entrainment by high velocity water jets. *Chem. Engng Sci.* **28**, 1161–1168.

Van de Sande, E. & Smith, J. M. 1976 Jet break-up and air entrainment by low velocity turbulent water jets. *Chem. Engng Sci.* **31**, 219–224.

Van Dyke, M. 1982 *Album of Fluid Motion*. Parabolic Press, Stanford.